ACS NANO

www.acsnano.org

ARTICLE

Dual Active Sites of Embedded Ni and Surface Frustrated Lewis Pairs on $CeO_2(110)$ for Efficient Photocatalytic CO_2 Methanation

Xiaolei Guo,[⊥] Yuqi Wu,[⊥] Yuhang Shao, Shengrong Zhou, Hui Song,* Yasuo Izumi, Liangwei Deng, Wenguo Wang, Jinlu He,* and Hongwei Zhang*

Cite This: *ACS Nano* 2025, 19, 38004−38015

Read Online

ACCESS | Metrics & More | Article Recommendations | Supporting Information

ABSTRACT: **Developing efficient catalysts to drive the Sabatier reaction under mild conditions remains a grand challenge. Here we present an "embedded dual active site" strategy that exploits the strong metal−support interaction (SMSI) on the $CeO_2(110)$ surface to stabilize Ni nanoparticles, effectively integrating frustrated Lewis pair (FLP, $Ce^{3+}-O^{2-}$) sites for photocatalytic CO_2 activation with adjacent Ni sites for hydrogenation. Compared to shallow Ni embedding on $CeO_2(111)$, Ni nanoparticles are embedded significantly deeper in the $CeO_2(110)$ lattice. Concurrently, surface analyses reveal that $CeO_2(110)$ more readily generates FLPs (Ce^{3+} and oxygen vacancy pairs) than $CeO_2(111)$. The resultant Ni_{10}/CeO_2 photocatalyst delivers a CH_4 production rate of 2402.6 $\mu mol \cdot g^{-1} \cdot h^{-1}$ under UV−visible light irradiation, far exceeding the performance of control catalysts constructed on $CeO_2(111)$. In situ diffuse reflectance infrared Fourier transform spectroscopy (DRIFTS) and density functional theory (DFT) calculations reveal a synergistic mechanism involving enhanced surface CO_2 adsorption (adsorption energy lowered to ∼ −1.2 eV), efficient photocarrier separation, and reduced kinetic barriers for reaction intermediates, greatly promoting CO_2 activation, and subsequent hydrogenation.**

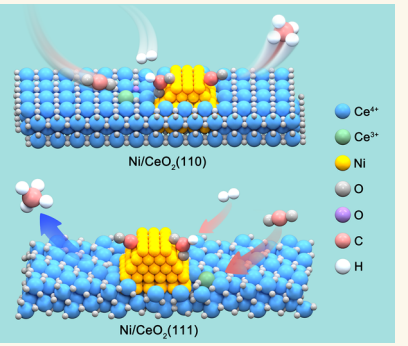

KEYWORDS: *photocatalytic, CO_2 methanation, Ni metal, CeO_2, frustrated Lewis pairs*

INTRODUCTION

Rising atmospheric CO_2 levels (422.8 ppm in 2024) from fossil-fuel-driven industrial activity are pushing us toward a climate tipping point. In this urgent context, CO_2 methanation (the Sabatier reaction) has attracted attention for its dual benefits of carbon-negative operation and energy storage. However, the conventional Sabatier process relies on high temperatures (300−500 °C) and high pressures to overcome the formidable C═O bond dissociation barrier (∼750 kJ·mol^{-1}), leading to high energy consumption and costs. Photocatalysis offers a promising alternative by directly converting CO_2 to easily storable methane (CH_4) under solar light at near-ambient conditions, especially when coupled with green hydrogen, thus enabling a zero−carbon cycle. Unfortunately, photocatalytic CO_2 hydrogenation is severely limited by sluggish CO_2 activation kinetics and rapid photocarrier recombination, resulting in low activity and selectivity. Overcoming these bottlenecks calls for innovative catalyst designs that integrate highly effective CO_2 activation and hydrogenation functionalities.[1−3]

Frustrated Lewis pairs (FLPs), spatially separated Lewis acid/base sites that remain reactive—have emerged as a powerful approach to activate inert molecules. In a typical FLP system, a Lewis acid site with an empty orbital and a Lewis base site with a lone pair are kept apart by steric hindrance. The Lewis acid can bind a CO_2 molecule via the oxygen, inducing charge polarization, while the neighboring Lewis base donates into the antibonding orbital to weaken the C═O bond (lengthening it by ∼0.12 Å), thereby cooperatively lowering the dissociation energy to ∼450 kJ·mol^{-1}.[4] Notably, the $CeO_2(110)$ crystal surface, owing to its unique facile oxygen vacancy migration, can spontaneously form a high density of FLPs ($Ce^{3+}-O$ vacancy pairs). This endows $CeO_2(110)$ with exceptional performance in thermal CO_2 conversion: for example, FLPs on $CeO_2(110)$ enabled >95% cyclic carbonate yield in cycloaddition of CO_2 with olefins,[5] and Pt−$CeO_2(110)$ interfacial engineering improved reverse

Received: July 31, 2025
Revised: October 17, 2025
Accepted: October 17, 2025
Published: October 23, 2025

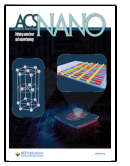

https://doi.org/10.1021/acsnano.5c12967
ACS Nano 2025, 19, 38004−38015

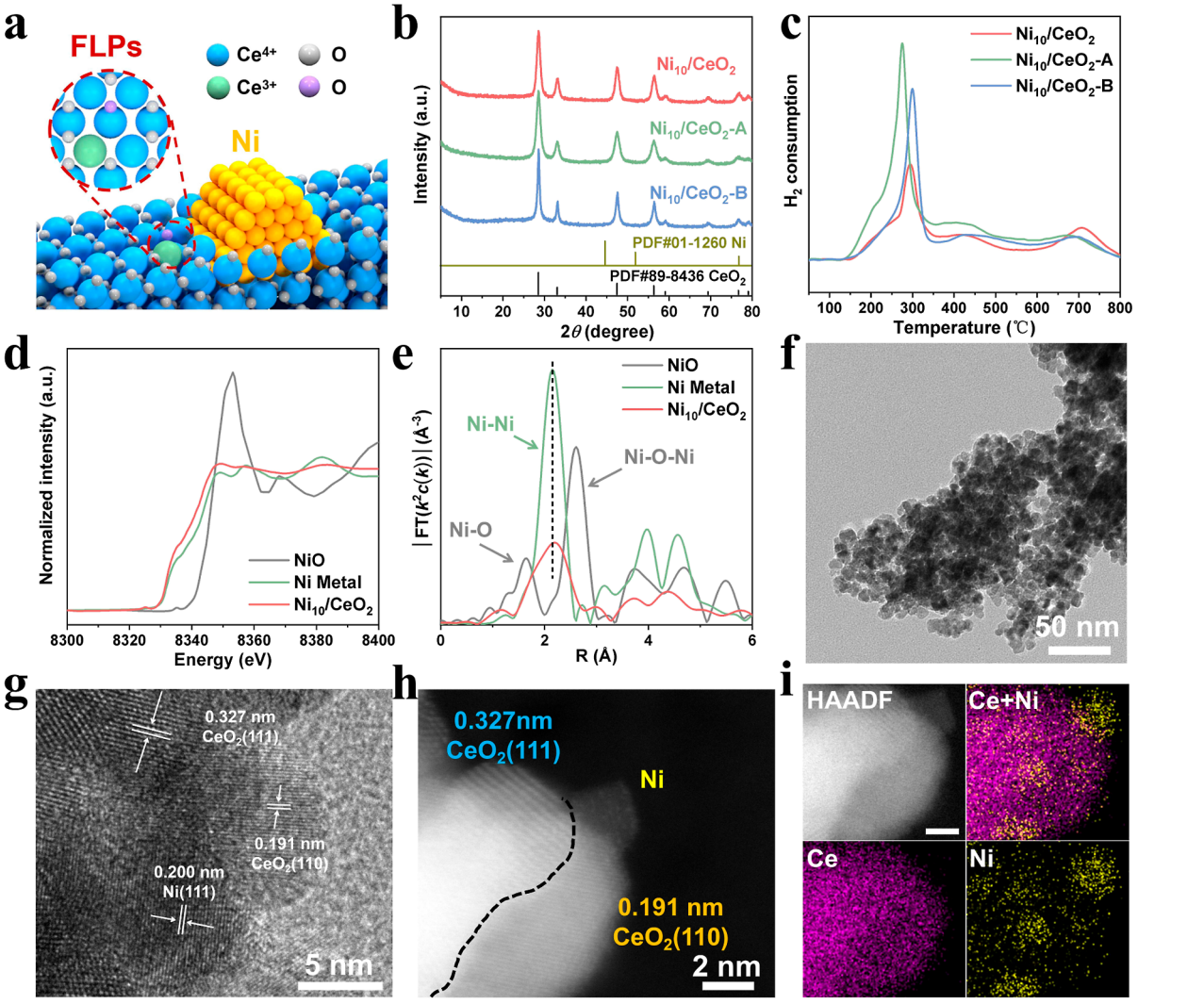

Figure 1. (a) Schematic illustration of embedded Ni nanoparticles and surface frustrated Lewis pairs (FLPs) on $CeO_2(110)$. (b) XRD patterns of Ni_{10}/CeO_2, Ni_{10}/CeO_2–A, and Ni_{10}/CeO_2–B. (c) H_2-TPR profiles. (d,e) Ni K-edge X-ray absorption near-edge structure (XANES, d) and extended X-ray absorption fine structure (EXAFS, e) spectra of Ni_{10}/CeO_2 and related materials. (f,g) TEM images of Ni_{10}/CeO_2. (h,i) Aberration-corrected HAADF-STEM image and corresponding EDS elemental mappings for Ni, Ce, and O, where the scale bar indicates 2 nm.

water–gas shift (RWGS) CO selectivity to 29.6%.[6] However, the potential of FLPs for photodriven CO_2 activation remains underexplored, and the underlying reaction mechanisms are not yet fully understood.

Meanwhile, recent studies in thermal catalysis have discovered an embedded metal structure at the interface of Pt and the $CeO_2(110)$ surface. This SMSI-induced embedding alters the catalyst's electronic structure and adsorption properties, promoting low-temperature water–gas shift reaction (WGSR) activity.[7−9] Therefore, in metal–oxide catalyst systems, SMSI-induced metal embedding may concomitantly generate FLP effects. The synergy between these two phenomena merits joint investigation, as it can reshape the catalyst's local geometric and electronic structures, thereby modulating CO_2 adsorption and activation. In this strategy, Ni nanoparticles are embedded into the CeO_2 support via strong metal–support interactions, and are positioned in close proximity (<2 nm) to FLP sites on the $CeO_2(110)$ surface. By precisely tuning the Ni embedding depth and the density of surface FLPs on $CeO_2(110)$, we construct a bifunctional interface wherein FLPs serve as CO_2 activation sites and embedded Ni serves as H_2 dissociation/hydrogenation sites. This intimate configuration harnesses the strengths of both components: the FLPs enable efficient low-temperature CO_2 dissociation, while the Ni nanoparticles—with their d-band center shifted upward by ∼0.7 eV due to strong coupling with CeO_2—provide optimized H adsorption energetics, accelerating hydrogen spillover and intermediate hydrogenation.

In this study, the $Ni_{10}/CeO_2(110)$ catalyst, prepared by embedding Ni nanoparticles into CeO_2, achieves a CH_4 production rate of 2402.6 $\mu mol \cdot g^{-1} \cdot h^{-1}$ under UV–visible light with nearly 100% CH_4 selectivity. This activity represents a significant enhancement over previously reported photocatalysts (by nearly an order of magnitude) and far exceeds that of control samples where Ni is supported on $CeO_2(111)$ surfaces (denoted Ni_{10}/CeO_2–A and Ni_{10}/CeO_2–B; see Supporting Information 1.1 for preparation details). Through comprehensive multiscale characterization and DFT simulations, we reveal that the exceptional performance arises from a triple synergistic effect: (1) the $CeO_2(110)$ facet generates

https://doi.org/10.1021/acsnano.5c12967
ACS Nano 2025, 19, 38004−38015

abundant surface oxygen vacancies (54.6% of O species) and Ce^{3+} centers (31.0% of Ce) to dramatically strengthen CO_2 adsorption (adsorption energy lowered to ~ −1.2 eV); (2) embedded Ni nanoparticles form a strongly coupled interface with CeO_2 (with ~0.8 e^- charge transfer per Ni atom), greatly enhancing light absorption and photothermal conversion (surface temperature reaching ~170 °C under 1.5 W·cm^{-2} illumination); (3) the subnanometer proximity of the two active sites (<2 nm) shortens the transfer distance for reaction intermediates (enabling migration on the order of microseconds), achieving kinetic matching between CO_2 activation and subsequent hydrogenation steps. This work not only demonstrates a high-performance photocatalyst for CO_2 methanation under mild conditions, but also provides a broadly applicable framework for the design of multiactive-site synergistic catalytic systems through atomic-level engineering of active sites.

RESULTS AND DISCUSSION

Catalyst Synthesis and Structure. A series of Ni/CeO_2 catalysts were synthesized by first preparing CeO_2 supports via a controlled sol−gel route and then depositing Ni by $NaBH_4$ reduction. CeO_2 precursors were calcined at 500 °C for 2 h to obtain highly crystalline CeO_2 nanoparticles (~15 nm), onto which 10 wt % Ni was loaded and annealed in H_2 at 450 °C to form the embedded structure, denoted Ni_{10}/CeO_2. To investigate the effect of support morphology, two control CeO_2 supports were prepared by calcination at 400 °C (CeO_2−A) and 600 °C (CeO_2−B) under otherwise identical conditions, and a commercial CeO_2 (CeO_2−C) was included as a reference. All samples were confirmed by inductively coupled plasma optical emission spectroscopy (ICP-OES) to have similar Ni loadings (7.54−8.06 wt %), ensuring that differences in performance arise from structural factors rather than composition (Table S1).

Figure 1a illustrates the proposed structure: Ni nanoparticles are embedded into the CeO_2(110) surface, adjacent to surface FLP sites (paired Ce^{3+} and O^{2-} defect sites). Powder X-ray diffraction (XRD, Figures 1b and S1) patterns for all samples display only fluorite-phase CeO_2 reflections (JCPDS #89-8436), with characteristic peaks at 2θ = 28.5° (111), 33.1° (200), and 47.5° (220). Among the three samples, Ni_{10}/CeO_2 exhibits the weakest intensity at the (111) reflection, indicating a lower relative proportion of the CeO_2(111) facet. Moreover, for the fluorite structure of CeO_2 (space group $Fm\bar{3}m$), the (110) reflection is forbidden and therefore does not appear in the XRD pattern. Considering the limitations of XRD analysis, further characterization via transmission electron microscopy (TEM) is necessary. No diffraction peaks corresponding to metallic Ni (2θ = 44.5°) or NiO (2θ = 37.3°) are observed even up to 20 wt % Ni loading, indicating that Ni is highly dispersed and likely incorporated in the CeO_2 lattice rather than existing as large separate crystallites.[7,10] This suggestion of sublattice Ni incorporation (embedding) is further probed by H_2-temperature-programmed reduction (H_2-TPR) and XPS analysis.

H_2-TPR profiles (Figures 1c and S2) reveal characteristic reduction peaks for pure CeO_2 at ~350−600 °C (surface oxygen reduction) and ~750 °C (bulk oxygen reduction). Upon Ni loading, all reduction features shift to lower temperature by 50−100 °C due to hydrogen spillover from Ni to CeO_2. Notably, Ni_{10}/CeO_2 and Ni_{10}/CeO_2−B exhibit an additional distinct reduction peak at ~300 °C,[11] attributable to the reduction of NiO species. In contrast, Ni_{10}/CeO_2−A shows a NiO reduction peak at an even lower temperature (~275 °C) with a much larger area (1.5 times that of Ni_{10}/CeO_2). The lower reduction temperature and higher peak intensity for Ni_{10}/CeO_2−A indicate a weaker metal−support interaction (MSI) in that sample, leading to more Ni remaining on or near the surface (less embedded).[12] In addition, the BET surface areas of CeO_2−A (177.9 m^2·g^{-1}) and CeO_2−B (117.3 m^2·g^{-1}) exceed that of CeO_2 (78.4 m^2·g^{-1}), indicating smaller crystallites and a larger fraction of surface lattice oxygen (Figure S3 and Table S2). The enhanced intensity of the first low-temperature TPR peak correlates with this trend and is consistent with Ni-driven hydrogen spillover promoting CeO_2 surface-oxygen reduction. This conclusion is consistent with XPS results: all Ni/CeO_2 samples show only very weak Ni 2p signals (Figure S4), and the Ni $2p_{3/2}$ binding energy (BE) is positively shifted by $\Delta_{BE} \approx 0.5$ eV relative to metallic Ni. Such a shift suggests Ni exists in an electron-deficient state (denoted $Ni^{\delta+}$) embedded in the CeO_2 lattice, with Ni_{10}/CeO_2 exhibiting the greatest embedding depth. These findings corroborate that Ni in Ni_{10}/CeO_2 is not simply surface-deposited but is integrated into the CeO_2 near-surface structure to a significant extent.[10,13] Meanwhile, BET results (Figure S3 and Table S2) show that compared to CeO_2, both CeO_2−A and CeO_2−B exhibit larger specific surface areas. After loading Ni, the specific surface areas of both CeO_2−A and CeO_2−B decreased significantly, accompanied by a corresponding reduction in pore volume, indicating that Ni nanoparticles physically blocked and covered the high-surface-area pore channels of the supports. In particular, the more pronounced decrease in Ni_{10}/CeO_2−B is related to its larger Ni nanoparticle size (7.3 nm) (Figure S5). It is worth noting that for CeO_2, the changes in specific surface area and pore volume before and after Ni loading were minimal, further supporting the deeper embedding of Ni in Ni_{10}/CeO_2, which is consistent with the H_2-TPR results.

To probe the local atomic structure and electronic state of the embedded Ni, we performed Ni K-edge X-ray absorption fine structure (XAFS) analysis (Figure 1d,e). The Ni K-edge XANES spectra (Figure 1d) show that Ni_{10}/CeO_2 has a pronounced white-line feature and pre-edge trend intermediate between metallic Ni and NiO standards. Detailed analysis indicates a substantial electron transfer from Ni to CeO_2, resulting in a partially oxidized interfacial Ni state (Ni^0/Ni^{2+} coexisting). This electronic charge transfer at the interface is a hallmark of strong metal−support interaction and modifies the d-band electronic structure of Ni. The Fourier-transformed EXAFS (Figure 1e) and fitted parameters (Table S3) further reveal that the first coordination shell of Ni is dominated by Ni−Ni contributions at $R \approx 2.15$ Å (no phase-corrected) with coordination number (C.N.) of 3.28 (Figure S6). However, the Ni−Ni bond distance is slightly longer than in bulk Ni, likely due to lattice strain from Ni−O−Ce interactions at the interface. Additionally, we identify contributions from Ni−O bonds at $R \approx 1.64$ Å (low coordination number) and a weak Ni−O−Ni interaction at $R \approx 2.61$ Å. More significantly, a distinct Ni−O−Ce peak appears around $R \approx 3.0$ Å, confirming that Ni atoms are in close contact with cerium atoms through bridging oxygen (forming Ni−O−Ce linkages at the embedded interface). These unique coordination environments not only stabilize the active Ni species against sintering, but also modulate the Ni electronic structure via metal−support charge transfer.[14−16] TEM and HAADF-STEM provide direct visual

https://doi.org/10.1021/acsnano.5c12967
ACS Nano 2025, 19, 38004−38015

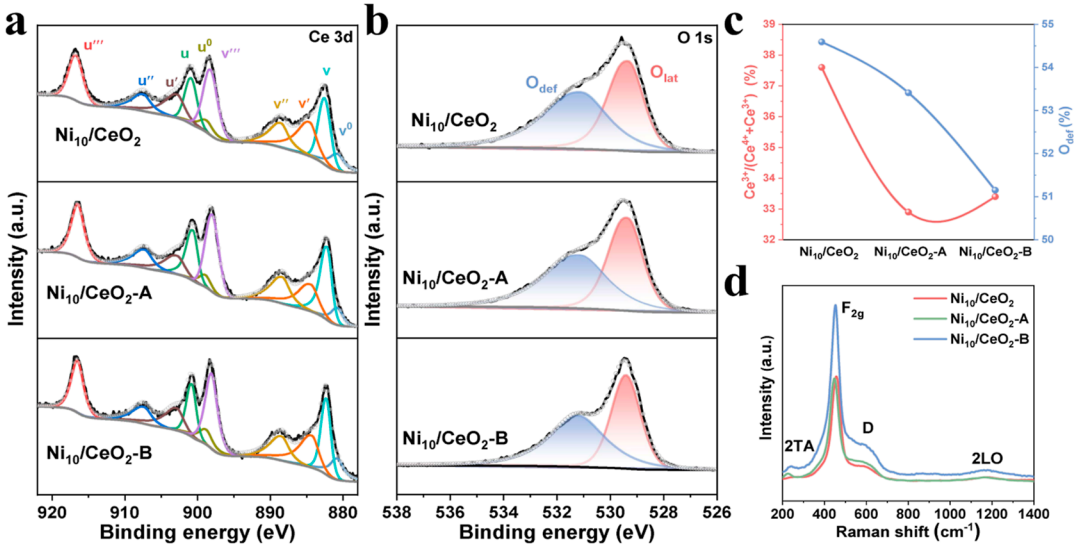

Figure 2. (a) Ce 3d and (b) O 1s XPS spectra of Ni_{10}/CeO_2 series photocatalysts. (c) Relative content of critical FLP components (Ce^{3+} and O_{def}) quantified from XPS analysis. (d) Raman spectra of the Ni_{10}/CeO_2 photocatalyst series.

evidence of the Ni embedding and the role of CeO_2 crystal facets (Figure 1f–i). High-resolution TEM images of Ni_{10}/CeO_2 (Figure 1 g) clearly show the CeO_2(110) lattice fringes (d = 0.191 nm) intimately juxtaposed with Ni(111) fringes (d = 0.200 nm). The aberration-corrected HAADF-STEM combined with energy-dispersive spectroscopy (EDS) further confirmed Ni embedding on both the CeO_2 (110) surface (Figures 1h,i and S7) and the CeO_2 (111) surface (Figure S8). Edge-resolved EDS line scans revealed a higher proportion of Ni nanoparticle embedding on the CeO_2 (110) surface, which is consistent with the H_2-TPR results. Subsequently, a quantitative statistical analysis was performed on the exposure ratios of the CeO_2(111) and CeO_2(110) facets across large-area HRTEM images for all three catalysts. The results show that the CeO_2(110) exposure fraction in Ni_{10}/CeO_2 reaches 51.2%, the highest among the samples (Figure S9), which is conducive to constructing efficient FLP sites. This indicates that Ni nanoparticles preferentially embed into the more reactive CeO_2(110) surface, establishing a coherent interface between Ni(111) and CeO_2(110) facets. In Ni_{10}/CeO_2–A (CeO_2 calcined at 400 °C), the CeO_2 is less crystalline and we observe some localized Ni nanoparticle aggregates (Figure S10), suggesting insufficient crystallinity led to poorer Ni dispersion/embedding. In Ni_{10}/CeO_2–B (CeO_2 calcined at 600 °C), the CeO_2 particles are larger and Ni appears partially encapsulated or buried due to excessive sintering of the support (Figure S11), which likely limits the formation of surface FLPs. By contrast, Ni_{10}/CeO_2 achieves an optimal embedding: Ni particles are anchored in the (110) facets with a tight interface. The spatial proximity between FLP sites (surface Ce^{3+}–O^{2-} pairs) and Ni hydrogenation sites in Ni_{10}/CeO_2 creates an efficient tandem catalytic pocket. This arrangement is ideal for photogenerated charge carrier transfer and intermediate shuttling between the two sites.[7,17] Aberration-corrected HAADF-STEM coupled with energy dispersive X-ray spectroscopy (EDS) mapping (Figure 1i) confirms the uniform distribution of Ni within the CeO_2 host, with Ni signals overlapping CeO_2 at the nanoscale, consistent with an embedded configuration.

Surface Electronic Structure and Oxygen Vacancies. Figure 2 examines how Ni embedding influences the CeO_2 surface electronic structure and oxygen vacancy distribution. We examined the Ce 3d and O 1s X-ray photoelectron spectra (XPS) of the Ni_{10}/CeO_2 series (Figure 2a–c). All peaks were energy-calibrated against the C 1s peak of adventitious carbon at 284.8 eV. For reference, the Ce 3d spectrum of pristine CeO_2 is provided in Figure S12a, where "v" represents the Ce $3d_5/_2$ orbitals and "u" represents the Ce $3d_3/_2$ orbitals. The peaks at 880.8 eV (v^0), 882.2 eV (v), 898.8 eV (u^0), and 900.5 eV (u) are assigned to Ce^{3+}, whereas those at 883.6 eV (v′), 888.6 eV (v″), 897.9 eV (v‴), 901.8 eV (u′), 907.5 eV (u″), and 916.4 eV (u‴) are attributed to Ce^{4+}(Figure 2a).[18,19] The Ce 3d spectrum of Ni_{10}/CeO_2 shows a markedly higher fraction of Ce^{3+} species: the ratio $Ce^{3+}/(Ce^{3+}+Ce^{4+})$ is 37.6%, compared to 29.1% in pure CeO_2. Additionally, After calibration to C 1s = 284.8 eV, the Ce 3d peaks of Ni_{10}/CeO_2 remain shifted to higher binding energy (~0.4 eV) relative to pristine CeO_2, indicative of a more electron-deficient Ce environment. These XPS features imply that embedding Ni into CeO_2 induces electron transfer from Ce to Ni (consistent with XANES), thereby increasing the concentration and stabilizing Ce^{3+} sites on the surface. The effect is especially pronounced for the CeO_2(110)-dominant sample, owing to the greater lattice relaxation and defect accommodation capacity of the (110) facet.[5,6]

Ni_{10}/CeO_2 exhibits a very high O_{def} fraction of 54.6% ($O_{def}/(O_{lat} + O_{def})$), which is significantly greater than the 38.6% in pure CeO_2. These surface oxygen vacancies (denoted S–O_V) are a key component of FLPs on CeO_2. Their presence can strongly polarize adsorbed CO_2 molecules, DFT calculations show an adsorption energy of −1.78 eV for CO_2 at an FLP site, significantly weakening the C═O bond.[20] In contrast, Ni_{10}/CeO_2–B (with predominantly CeO_2(111) facets) has lower Ce^{3+} ratio (33.4%) and O_{def} fraction (51.2%) than Ni_{10}/CeO_2 (Figure 2c, Tables S4 and S5). This confirms the crucial role of the CeO_2 surface orientation: CeO_2(110) is inherently more prone to form FLPs (Ce^{3+} and O vacancy pairs) than CeO_2(111).

We further investigated the relationship between bulk oxygen vacancies and the crystal facet/Ni embedding via electron paramagnetic resonance (EPR) and Raman spectroscopy (Figures 2d and S13, S14). EPR is sensitive to

https://doi.org/10.1021/acsnano.5c12967
ACS Nano 2025, 19, 38004–38015

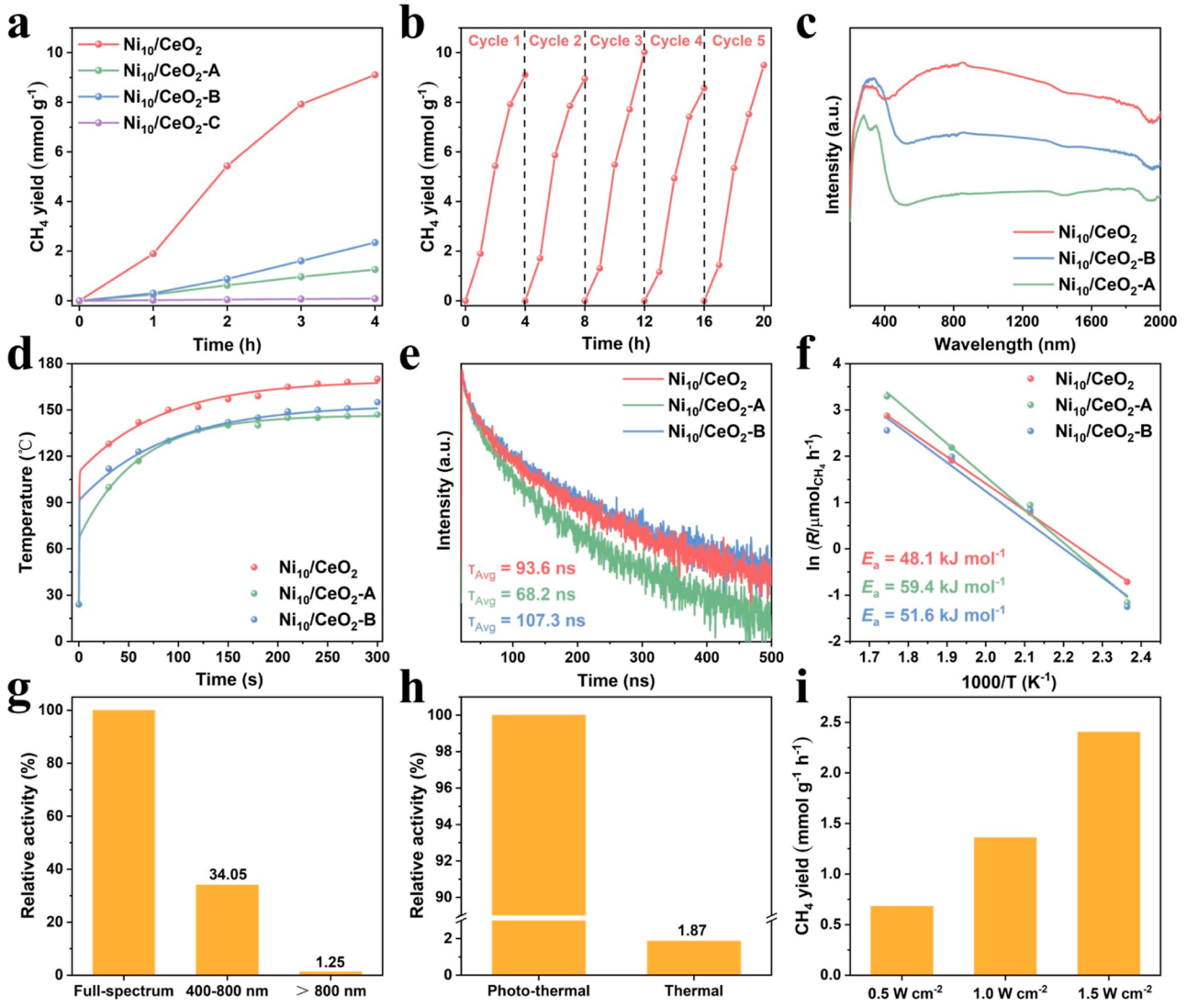

Figure 3. (a) Photocatalytic CO_2 methanation activity of Ni_{10}/CeO_2, Ni_{10}/CeO_2−A, Ni_{10}/CeO_2−B, and Ni_{10}/CeO_2−C under irradiation (1.5 W·cm^{-2}). (b) Cycling stability of Ni_{10}/CeO_2 over 20 h reaction. (c) UV−vis absorption spectra of catalysts. (d) Surface temperature evolution under reaction irradiation. (e) TRPL decay curves. (f) Arrhenius plots for CH_4 production over the catalysts. Dependence of activity using Ni_{10}/CeO_2 on (g) light wavelength, (h) thermal effects and (i) light intensities.

paramagnetic Ce^{3+} centers associated with oxygen vacancies. EPR analysis shows that Ni_{10}/CeO_2−B (with mostly (111) facets) has the highest bulk oxygen vacancy concentration (denoted B−O_V, reflecting Ce^{3+} in the lattice) because CeO_2(111) has a lower formation energy for bulk oxygen vacancies (~2.1 eV). Remarkably, Ni_{10}/CeO_2 (110 facet, deeply embedded Ni) achieves a bulk vacancy concentration nearly as high as Ni_{10}/CeO_2−B, despite the (110) facet's intrinsically higher vacancy formation energy, presumably through the enhanced hydrogen spillover effect of embedded Ni. This level is significantly above that of Ni_{10}/CeO_2−A (shallow Ni embed). The trend in B−O_V (Ni_{10}/CeO_2−B ≥ Ni_{10}/CeO_2 ≫ Ni_{10}/CeO_2−A) parallels the earlier H_2-TPR observation that Ni_{10}/CeO_2−A had the least embedded Ni and largest NiO reduction peak (indicating more NiO on surface). In other words, deeper Ni embedding correlates with greater activation of the CeO_2 lattice (bulk vacancy generation) up to the level seen in the inherently vacancy-rich (111) facet.[21,22]

Raman spectroscopy further corroborates these conclusions. All Ni-embedded CeO_2 samples display an intensified defect-induced mode (D, around 590 cm^{-1}) and a weakened F_{2g} mode (symmetric Ce−O stretch of fluorite CeO_2 at 457 cm^{-1}) compared to undoped CeO_2.[13,17,23] The intensity ratio (I_D/I_{F2g}) follows Ni_{10}/CeO_2−B (0.33) > Ni_{10}/CeO_2 (0.30) > Ni_{10}/CeO_2−A (0.29), in excellent agreement with the bulk vacancy concentrations from EPR. The increase in D band and decrease in F_{2g} indicate the creation of oxygen defect sites in the CeO_2 lattice upon Ni embedding. Mechanistically, embedding Ni nanoparticles induces hydrogen spillover under reaction conditions, whereby H atoms migrate onto CeO_2 and reduce Ce^{4+} to Ce^{3+}, generating oxygen vacancies. This spillover effect weakens Ce−O bonds and triggers the formation of bulk vacancies. Notably, in Ni_{10}/CeO_2, the Raman 2TA overtone mode at ~262 cm^{-1} disappears, which is attributed to lattice distortion from the interfacial stress caused by the embedded Ni−CeO_2 interface. Such an interfacial stress field can, via a piezoelectric-like effect, influence charge carrier separation and extend photocarrier lifetimes (as discussed later). Moreover, the F_{2g} peak in Ni_{10}/CeO_2 is shifted by $\Delta\omega$ ≈ 2.0 cm^{-1} relative to pure CeO_2, which quantitatively reflects

https://doi.org/10.1021/acsnano.5c12967
ACS Nano 2025, 19, 38004−38015

differences in Ni incorporation and lattice strain (Figure S14).[24,25] We note that Raman spectroscopy with an excitation wavelength of 532 nm primarily reports bulk-sensitive vacancy signatures, which explains its alignment with EPR and the divergence from the surface-weighted XPS results.

In summary, CeO_2(110)-supported Ni exhibits a strong tendency to concentrate oxygen vacancies at the surface (forming FLPs for CO_2 binding) while simultaneously, deep Ni embedding and facet effects govern the bulk vacancy population. The Ni_{10}/CeO_2 catalyst (high FLP density on (110), deeply embedded Ni) thus optimizes both surface and bulk defect states, which is expected to be highly beneficial for CO_2 activation and photocarrier dynamics.

Photocatalytic Performance and Photothermal Effects. We evaluated the photocatalytic CO_2 hydrogenation ($CO_2 + 4H_2 \rightarrow CH_4 + 2H_2O$) performance of Ni_{10}/CeO_2 against the control samples under UV−visible light irradiation (λ = 200−2500 nm, intensity 1.5 W·cm^{-2}). The reaction was carried out in a sealed glass loop reactor with a feed gas of Ar/H_2/CO_2 = 10:9:1 at near ambient temperature and under light irradiation for at least 4 h. As shown in Figures 3a and S10, Ni loading was optimized among Ni loadings from 0 to 20 wt %, the 10 wt % Ni catalyst gave the highest activity (Figure S15). The Ni_{10}/CeO_2 exhibits an exceptional CH_4 production rate of 2402.6 μmol·g^{-1}·h^{-1} under illumination, which is ∼890 times higher than that of pure CeO_2 (only ∼2.7 μmol·g^{-1}·h^{-1}, essentially negligible), the turnover number (TON) of the Ni_{10}/CeO_2 catalyst is approximately 5.7. It also vastly outperforms Ni_{10}/CeO_2−A, Ni_{10}/CeO_2−B, and Ni_{10}/CeO_2−C, which produce much lower CH_4 rates under identical conditions (Figure 3a). This dramatic enhancement underscores the effectiveness of the embedded dual-site strategy on CeO_2(110). In control tests without light, no measurable CH_4 was produced, confirming that the reaction is indeed photocatalytic (with possible photothermal contribution). The CH_4 selectivity on Ni_{10}/CeO_2 was nearly 100%, with no CO and other products detected, indicating nearly complete selectivity to Sabatier reaction over reverse water−gas shift.

The superior activity of Ni_{10}/CeO_2 can be attributed to the synergistic interaction between FLPs and embedded Ni. The FLP sites on CeO_2(110) polarize and activate CO_2, lowering the activation energy for CO_2 dissociation, while the Ni sites facilitate H_2 dissociation and hydrogenation steps. DFT analysis (discussed later) reveals that the Ni−CeO_2(110) interface has an upshifted Ni d-band center (and Fermi level) compared to a nonembedded case, which improves Ni's binding with hydrogen intermediates and accelerates H spillover to the CeO_2 surface. This synergistic "FLP activation and Ni hydrogenation" mechanism effectively bridges the gap between CO_2 and H_2 activation, enabling much faster kinetics than either component alone could achieve. Importantly, Ni−CeO_2(110) also exhibited excellent stability, with no noticeable loss of activity over 5 reaction cycles (20 h cumulative, Figure 3b). Also, the XRD patterns and TEM images of the Ni−CeO_2(110) catalyst after five reaction cycles closely resemble those of the fresh catalyst, indicating excellent structural stability (Figures S16 and S17). This stability is attributed to the embedded Ni structure, which suppresses Ni particle sintering and oxidation under reaction conditions.

The enhanced light-harvesting and photothermal conversion of the catalysts were examined by UV−Vis diffuse reflectance spectroscopy and infrared thermography (Figure 3c,d). UV−Vis diffuse reflectance spectra (Figure 3c) show that with increasing Ni loading, the absorption edge of the catalysts showed a significant redshift, expanding from 410 nm for pure CeO_2 to 650 nm for Ni_{20}/CeO_2, along with notably enhanced absorption in the infrared region (800−2000 nm, Figure S18).[22] Ni_{10}/CeO_2 has significantly enhanced visible-light absorption compared to pure CeO_2, Ni_{10}/CeO_2−A, and Ni_{10}/CeO_2−B, which may be attributed to the smaller particle sizes of Ni and CeO_2 and abundant surface oxygen vacancies that facilitate photon capture, as similarly reported for dark-colored defect-engineered materials like In_2O_3 and TiO_2.[26,27] The dark brown color of Ni_{10}/CeO_2 indicates strong light harvesting, which can generate more electron−hole pairs and photothermal heat. Consistently, under reaction light intensity, Ni_{10}/CeO_2's surface temperature (measured by IR thermography, Figure S19) rises to ∼170 °C, which is about 51 °C higher than that of Ni_{10}/CeO_2−A/B (Figure 3d). We estimate Ni_{10}/CeO_2 achieves the highest photothermal conversion efficiency (η) among the series, supplying additional thermal energy to drive the endothermic CO_2 methanation reaction.

To gain insight into charge carrier dynamics and reaction energetics, we performed time-resolved photoluminescence (TRPL) and Arrhenius kinetic analysis (Figure 3e,f). TRPL measurements (Figure 3e) were conducted to probe photocarrier lifetimes, the PL decay curves (at 470 nm emission) were fitted with a biexponential model to extract average lifetimes. Ni_{10}/CeO_2 exhibits an average photocarrier lifetime of 93.6 ns, which is 13.5% longer than that of pure CeO_2 (82.4 ns). This extended lifetime indicates that photoexcited electrons and holes in Ni_{10}/CeO_2 recombine more slowly, likely due to charge separation at the Ni/CeO_2 Schottky junction.[28,29] The embedded Ni forms intimate contacts with CeO_2, creating Schottky barriers that attract photoelectrons and impede their direct recombination with holes in the semiconductor. Interestingly, Ni_{10}/CeO_2−B shows an even longer carrier lifetime (∼107.3 ns), possibly because CeO_2(111)'s higher bulk vacancy content can act as electron traps that prolong decay. However, those trapped electrons in bulk may be less accessible for reaction, whereas Ni_{10}/CeO_2 strikes a balance between improved separation and availability of electrons at the surface FLPs for CO_2 activation.

We determined apparent activation energies (E_a) for CH_4 production by running temperature-dependent reaction rates (Figure 3f). Ni_{10}/CeO_2 exhibits an E_a of 48.1 kJ·mol^{-1}, which is ∼30% lower than that of Ni_{10}/CeO_2−A (68.5 kJ·mol^{-1}). The reduced E_a on Ni_{10}/CeO_2 reflects the more favorable reaction pathway enabled by the CeO_2(110) FLPs and embedded Ni dual sites. In essence, the dynamic migration of oxygen vacancies (and thus the mobility of FLP sites) on CeO_2(110) creates a spatial confinement that pairs the CO_2 activation site and H species in close vicinity, thereby significantly lowering the energy barriers for intermediate steps. Hydrogen spillover from Ni to CeO_2 is facilitated, delivering H atoms directly to activated CO_2 species. These kinetic advantages are further illuminated by the mechanistic studies below.

To further elucidate the synergistic effect in the photothermal chemical reaction of the Ni_{10}/CeO_2 catalyst, the activity dependence under full-spectrum, visible light (400−800 nm), and infrared light (>800 nm) irradiation was investigated using optical cutoff filters (Figure 3g). The catalytic activities under visible and infrared light irradiation alone were 34.05% and 1.25%, respectively, compared to that under full-spectrum irradiation. This indicates that UV-driven

https://doi.org/10.1021/acsnano.5c12967
ACS Nano 2025, 19, 38004−38015

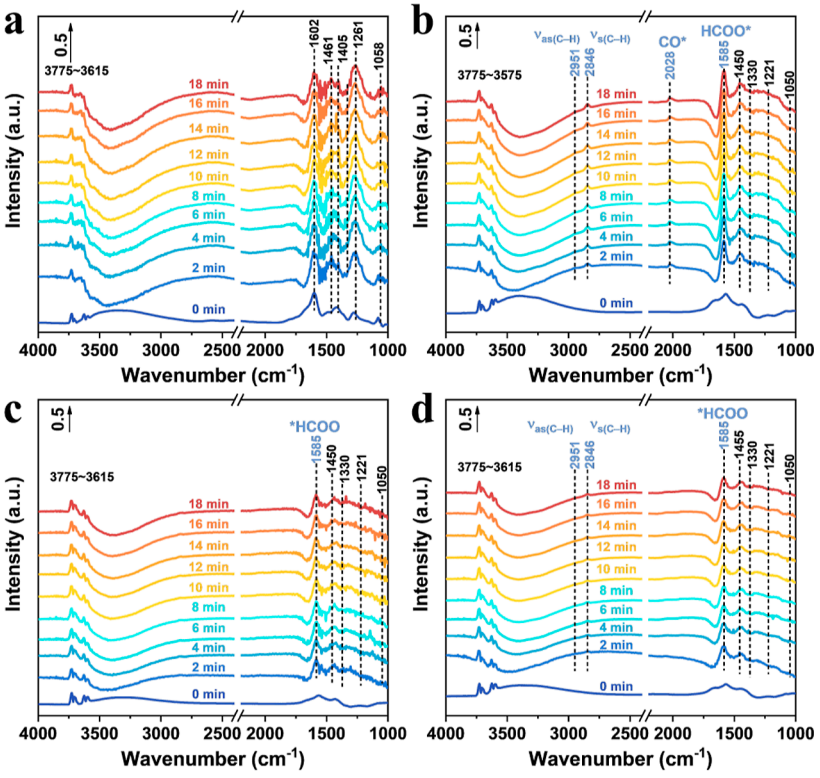

Figure 4. In situ DRIFTS spectra recorded during photocatalytic CO_2 methanation reaction on (a) CeO_2, (b) Ni_{10}/CeO_2, (c) Ni_{10}/CeO_2−A, and (d) Ni_{10}/CeO_2−B.

photogenerated electrons predominantly contribute to the reaction. Given the bandgap of Ni_{10}/CeO_2 is 1.94 eV (Figure S20), corresponding to an excitation wavelength of approximately 640 nm, partial visible light can also induce electron−hole pair separation. Meanwhile, the thermal electron contribution under infrared light (with the catalyst's corresponding surface temperature of 115 °C) is negligible. Additionally, a purely thermal catalytic test conducted in the dark at 170 °C (the surface temperature of Ni_{10}/CeO_2 under illumination, Figure 3h) showed activity only 1.87% of the full-spectrum reaction. Further validation was obtained by varying the illumination intensity (0.5−1.5 W/cm^{-2}), demonstrating a nearly linear relationship between reaction activity and intensity (Figure 3i). This confirms that photocatalytic electron/hole pairs play a dominant role, with the efficient photothermal synergy significantly enhancing catalytic activity. Photogenerated carriers from both photon and thermal excitation can directly inject electrons into the antibonding orbitals of CO_2, overcoming the reaction activation barrier and markedly accelerating reaction kinetics.

In Situ DRIFTS Mechanistic Studies. To gain insight into reaction intermediates and pathways, we performed in situ diffuse reflectance infrared Fourier transform spectroscopy (DRIFTS) during CO_2 hydrogenation under light. Figure 4a−c shows time-resolved DRIFTS spectra for Ni_{10}/CeO_2, Ni_{10}/CeO_2−A, and Ni_{10}/CeO_2−B during CO_2 + H_2 adsorption (prior to light) and subsequent photocatalytic reaction (under 1.0 W·cm^{-2} light). Corresponding spectra for bare CeO_2 and CeO_2−A/B without Ni are in Figure S23d−f for comparison.

In the adsorption phase (CO_2 + H_2 flowed in the dark), Ni_{10}/CeO_2 initially shows O−H stretches at 3575−3775 cm^{-1} due to surface −OH groups formed, these likely originate from dissociative adsorption of trace H_2O or H_2 on CeO_2. The intensity of these −OH band correlates with the amount of CO_2 adsorbed, as −OH can form from H_2 interacting with surface O. A broad O−H band below 3500 cm^{-1} appears, assignable to the O−H vibration of monodentate bicarbonate species.[30,31] Concurrently, several carbonyl and carbonate bands emerge: peaks at ∼1429 and 1570 cm^{-1} are attributed to bidentate carbonates, peaks at 1243, 1570, and 1669 cm^{-1} to monodentate bicarbonates, and a peak around 1083 cm^{-1} to another carbonate species.[32,33] These assignments agree with literature for CO_2 adsorbates on CeO_2. Notably, compared to bare CeO_2 (Figure S23a), Ni_{10}/CeO_2 shows generally weaker carbonate and bicarbonate bands (especially the bicarbonate at 1602 cm^{-1}). This indicates that the presence of embedded Ni and associated FLPs modifies the CO_2 adsorption mode. Temperature-programmed desorption of CO_2 (CO_2-TPD, Figure S24a) further reveals that Ni embedding greatly suppresses strongly bound CO_2 species desorbing at 500−800 °C, while enhancing moderately bound CO_2 that desorbs at 170−400 °C.[28] These results suggest Ni_{10}/CeO_2 favors a more active CO_2 adsorption configuration (likely via FLPs) that is easier to activate (not immobilized as unreactive carbonate salts). In short, embedding Ni into CeO_2 appears to optimize the adsorption strength and form of CO_2, avoiding unproductive bicarbonate buildup and promoting an adsorption state conducive to reaction.

Once the light is turned on to initiate the reaction, dramatic changes are observed, especially for Ni_{10}/CeO_2 (Figure 4b). The broad O−H band (<3500 cm^{-1}) from bicarbonate O−H disappears rapidly, indicating that the monodentate bicarbonate species are being consumed. The bands for carbonate and bicarbonate (e.g., 1429, 1570, 1669 cm^{-1}) become dynamic—some intensities decrease, and new bands grow in, signifying these intermediates are turning over. Two new peaks

https://doi.org/10.1021/acsnano.5c12967
ACS Nano 2025, 19, 38004−38015

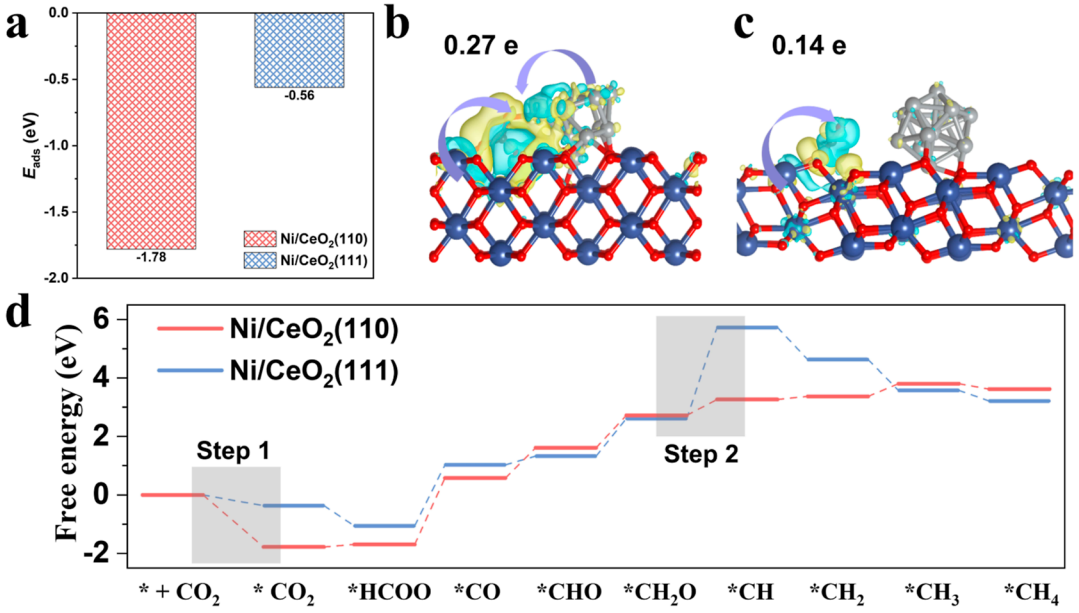

Figure 5. (a) DFT calculated CO_2 adsorption energies on Ni_{10}/CeO_2 (110) and Ni_{10}/CeO_2 (111) models. Charge-density difference maps of adsorbed CO_2 on (b) Ni_{10}/CeO_2 (110) and (c) Ni_{10}/CeO_2 (111), electron density accumulation (yellow) and depletion (cyan). Silver, blue, red, brown, and white spheres represent Ni, Ce, O, C, and H atoms, respectively. (d) Gibbs free energy diagrams for each step in the photocatalytic CO_2 methanation process over the two photocatalysts.

emerge at 1585 cm^{-1} and 2028 cm^{-1}.[34] The 1585 cm^{-1} band is assignable to formate species (HCOO*) adsorbed on CeO_2, while the 2028 cm^{-1} band is characteristic of linearly adsorbed CO on metallic Ni (Ni−CO stretching). The appearance of these peaks confirms a reaction pathway via formate intermediate: CO_2 initially forms carbonates/bicarbonates on CeO_2 (FLP sites), which are then hydrogenated to formate (HCOO*), and subsequently formate decomposes to CO* (probably on Ni) and/or directly to surface CO species. At longer reaction times, we observe growth of C−H stretch bands at 2967 cm^{-1} and 2886 cm^{-1}, corresponding to asymmetric and symmetric C−H stretches of *CH_x (methoxy, methyl, or methane precursor) species.[35] The presence of CH_x signals indicates progress toward methane formation on the catalyst surface. Importantly, Ni_{10}/CeO_2 exhibits relatively weak intensity of CH_4 adsorption bands compared to bare CeO_2. In fact, CH_4-TPD of the spent catalysts (Figure S24b) shows that Ni_{10}/CeO_2 adsorbs CH_4 much less strongly than pure CeO_2, which greatly facilitates CH_4 desorption and prevents site blocking by product.

The DRIFTS profiles for Ni_{10}/CeO_2 indicate that under illumination, CO_2 is initially captured and activated on CeO_2(110) FLP sites as carbonate/bicarbonate species; upon receiving hydrogen (from spillover or direct H_2 dissociation on Ni), these intermediates are converted to formate on the CeO_2 surface. Then the formate further converts to CO (likely at the interface or on Ni), and finally CO is rapidly hydrogenated on Ni to CH_x and then CH_4. The key point is that the interaction between Ni and FLPs enables a tandem reaction: CO_2 activation occurs on CeO_2, and hydrogenation occurs on Ni, with intermediates shuttling between the two.

For Ni_{10}/CeO_2−A and−B, DRIFTS (Figures 4c,d and S22b,c) shows similar types of intermediates but with notable differences in intensity. During adsorption, Ni_{10}/CeO_2−A and−B show the same set of carbonate/bicarbonate peaks as Ni_{10}/CeO_2, but generally weaker. Moreover, the CeO_2−A and CeO_2−B supports (without Ni, Figure S23b,c) show a pronounced absence of many carbonate/bicarbonate peaks in 1300−1550 cm^{-1} region, reflecting their much lower intrinsic CO_2 uptake due to fewer FLPs. This aligns with earlier XPS/EPR data that CeO_2−A/B have fewer surface vacancies. Under reaction conditions, both Ni_{10}/CeO_2−A and−B do produce formate (HCOO*) signals, but neither shows the Ni−CO band at ∼2020 cm^{-1}. The ν(C−H) bands (2967/2886 cm^{-1}) are observed in Ni_{10}/CeO_2−B but are barely detectable in Ni_{10}/CeO_2−A, suggesting Ni_{10}/CeO_2−B can proceed further along the pathway (to CH_x species) than Ni_{10}/CeO_2−A. The absence of CO* adsorption in both indicates a slower or limited formate to CO conversion on those catalysts, likely due to insufficient FLP activity to drive CO_2 fully to CO in tandem with Ni. Indeed, CeO_2(111)-dominant Ni_{10}/CeO_2−B, despite deeper Ni embed than −A, still has inherently less capability to activate CO_2 than CeO_2(110). The result is a rate bottleneck: on Ni_{10}/CeO_2−B, the conversion of formate to CO is the limiting step (since CO hydrogenation to CH_4 on Ni is fast), which caps the overall rate. Ni_{10}/CeO_2, with its stronger FLP sites, can convert formate to CO (and onward to CH_4) more readily, avoiding accumulation of formate and achieving higher overall rates.

The in situ DRIFTS spectra of Ni_{10}/CeO_2 under dark conditions at 170 °C revealed that carbonate and bicarbonate species became active after the initiation of the thermal reaction (1000−1560 cm^{-1}). Simultaneously, weakly adsorbed CO* was observed on the catalyst surface (Figure S25). This indicates that the activation of frustrated Lewis pairs (FLPs) and Ni hydrogenation can proceed under purely thermal conditions, although their reactivity is significantly lower compared to the corresponding photothermal conditions. Furthermore, the absence of key reaction intermediates such as *HCOO (1585 cm^{-1}) and ν(C−H) (2967/2886 cm^{-1}) during the reaction also demonstrates the insufficient hydrogenation capability of Ni under purely thermal conditions, which is consistent with the thermal performance results of Ni_{10}/CeO_2 (Figure 3g,h).

https://doi.org/10.1021/acsnano.5c12967
ACS Nano 2025, 19, 38004−38015

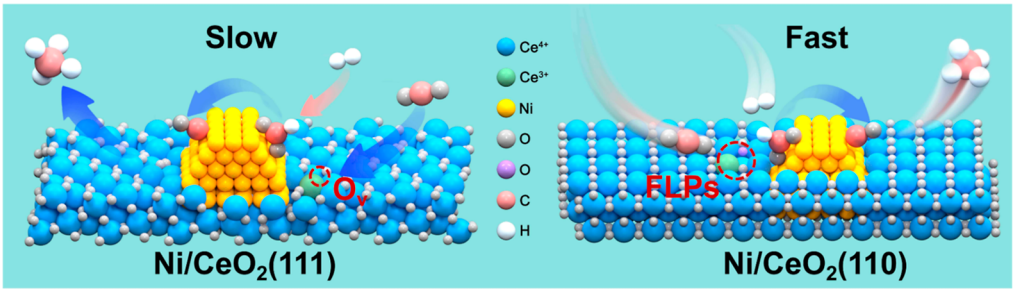

Figure 6. Schematic illustration of the mechanism of photocatalytic CO_2 methanation on the surfaces of Ni/CeO_2 (111) and Ni/CeO_2 (110).

DFT Calculations. To complement the in situ DRIFTS experiments and validate the proposed mechanism, we carried out DFT calculations for CO_2 activation and hydrogenation on Ni/CeO_2 models. We constructed two periodic models: Ni_{13} clusters supported on CeO_2(110) and on CeO_2(111). To simulate the embedded Ni structure, a Ni cluster was positioned in a surface oxygen vacancy site on each surface. Additionally, for the CeO_2(110) model we included a neighboring surface oxygen vacancy to represent the Ce^{3+}–O^{2-} FLP pair, whereas the CeO_2(111) model inherently can only host isolated oxygen vacancies (no FLP pair).[36−38] The optimized structures show a stark contrast: on CeO_2(110), the Ni cluster sinks into the surface, bonding strongly with surrounding O atoms and Ce cations (Figure S26a), indicative of a stable partially embedded configuration. On CeO_2(111), the Ni cluster remains mostly on top of the surface with much less penetration (Figure S26b), in line with our experimental finding of shallow Ni on (111). These models confirm that the (110) surface promotes a greater degree of Ni embedding via strong metal−support bonding, consistent with SMSI phenomena.

We then calculated CO_2 adsorption energies on both models. On Ni/CeO_2(110) with an FLP site (Figure 5a), CO_2 binds exothermically with E_{ads} = −1.78 eV, forming a carbonate-like coordination between a surface Ce^{3+} and an adjacent O vacancy site (O atom of CO_2 binds to Ce^{3+}, C atom interacts with Ni or nearby O). In contrast, on Ni/CeO_2(111) (single oxygen vacancy, no FLP), CO_2 adsorption is much weaker, E_{ads} = −0.56 eV. This approximately 3-fold stronger binding on the (110) dual-site surface directly demonstrates the benefit of FLPs for CO_2 capture and activation. The CO_2 molecule on Ni/CeO_2(110) is highly polarized: Bader charge analysis shows ∼0.27 |e| of electron density is transferred into the CO_2 molecule (populating its antibonding orbitals), whereas only 0.14 |e| is transferred to CO_2 on Ni/CeO_2(111). Notably, on Ni/CeO_2(110), the charge does not come solely from the Ni or solely from CeO_2, but from a cooperative donation by both the Ni cluster and the FLP site (Ce^{3+}−O vacancy). The electron density difference plots (Figure 5b,c) visualize this: a significant accumulation of electron density (yellow regions) is seen on the CO_2 molecule and at the interface, while depletion (cyan) is around the Ni and nearby Ce, illustrating a synergistic charge redistribution when both Ni and FLP are present. In essence, the FLP site activates CO_2 by donating into the molecule, and the Ni concurrently back-donates/accepts electron density, resulting in a highly activated CO_2 ad-species.

Finally, we examined the reaction energy profile for CO_2 methanation on both models (Figure 5d). The Gibbs free energy diagrams reveal the stepwise conversion: CO_2 → HCOO* → CO* → CH_3O* → CH_2O* → *CH → CH_4 (with intermediate hydrogenation steps). The rate-limiting step on both catalysts is the initial activation of CO_2 to form a $CO_2^{\delta-}$ adsorbate or transition state leading into formate. On Ni/CeO_2(110) with FLPs, this barrier is substantially lower than on Ni/CeO_2(111). This aligns with the experimental observation that FLPs greatly accelerate CO_2 activation. Moreover, at later stages of the reaction, the embedded Ni catalyst shows lower energy requirements for critical hydrogenation steps. In particular, the transformation of *CH_2O (a key intermediate, possibly surface formaldehyde or methoxy) to *CH (carbene or methyl species) is much more favorable on Ni/CeO_2(110). We find that the deeply embedded Ni and proximal FLP on CeO_2(110) stabilize the transition state and intermediate for this step, reducing its free energy change significantly compared to the (111) case (Figure 6). As a result, the overall pathway to CH_4 is energetically smoother on the dual-site catalyst. These theoretical findings corroborate our experimental observations and confirm the pivotal role of the dual-site synergy in boosting photocatalytic CO_2 methanation.

CONCLUSION

In summary, we have successfully constructed dual adjacent active sites consisting of surface FLPs and embedded Ni on the CeO_2(110) surface. The FLPs (Ce^{3+}−O^{2-} pairs) are responsible for CO_2 adsorption and activation, while the neighboring embedded Ni nanoparticles carry out subsequent hydrogenation steps. The strong synergy between these two sites greatly boosts the performance of the Ni_{10}/CeO_2 photocatalyst for the Sabatier reaction under light irradiation. Ni_{10}/CeO_2 achieves a high CH_4 production rate of 2402.6 $\mu mol \cdot g^{-1} \cdot h^{-1}$ with excellent stability. Furthermore, compared to CeO_2(111), the CeO_2(110) surface is far more effective in generating FLPs and accommodating embedded Ni. This unique structure notably enhances light absorption and photothermal conversion, while significantly lowering the energy barriers for CO_2 activation and intermediate hydrogenation, thereby enabling the reaction to proceed more efficiently at mild conditions. This study combined experimental and theoretical study provides fundamental insights into surface FLPs and embedded Ni active sites can be synergistically coupled, offering a new conceptual framework for the design of catalytic systems with multiple cooperative active sites.

EXPERIMENTAL METHODS

Materials. Nickel chloride hexahydrate ($NiCl_2 \cdot 6H_2O$, 99%), ammonia (25−28%), cerium nitrate ($Ce(NO_3)_4$, 99.9%), and CeO_2−Commercial (20−50 nm) were purchased from Shanghai

https://doi.org/10.1021/acsnano.5c12967
ACS Nano 2025, 19, 38004−38015

Maclin Biochemical Technology Co. Sodium borohydride ($NaBH_4$, AR) was purchased from Sinopharm Chemical Reagent Co. CeO_2-Type A (JRC-CEO-2, specific surface area 123.1 m^2/g, average pore size 7.08 nm) and CeO_2-Type B (JRC-CEO-3, specific surface area 81.4 m^2/g, average pore size 11.6 nm) were obtained from the Japan Society of Catalysis. All reagents were not purified before use.

Synthesis of CeO_2 Substrate. The CeO_2 substrate was synthesized through a room-temperature aqueous-phase method. Specifically, a predetermined amount of $Ce(NO_3)_4$ was dissolved in deionized water. Ammonia solution was then added dropwise to the mixture until the pH value of the solution reached 9. The solution was stirred at room temperature for 2 h and aged under static conditions for an additional 24 h. The resulting product was centrifuged and repeatedly washed with deionized water until the supernatant reached a neutral pH of 7. The separated powder was dried at 80 °C in air and subsequently calcined at 500 °C for 3 h to obtain the final CeO_2 substrate.

Synthesis of Ni/CeO_2 Photocatalysts. The Ni species were loaded onto the CeO_2 substrate via a sodium borohydride reduction method. In a typical synthesis process, a predetermined amount of CeO_2 substrate was dispersed in deionized water and ultrasonicated for 5 min to achieve homogeneous dispersion. The mixture was then stirred at 1000 rpm for 1 h. A corresponding volume of $NiCl_2$ aqueous solution (1 M) was added according to the target Ni mass fractions (1, 3, 10, or 20 wt %), followed by continuous stirring for an additional 1 h. Subsequently, a 10 mL $NaBH_4$ solution was prepared with a molar ratio of Ni: $NaBH_4$ = 1:8 and slowly introduced into the mixture via dropwise addition. After complete reduction, the sample was filtered, repeatedly washed with deionized water, and dried at 80 °C in air. Finally, the obtained powder was reduced under a 10% H_2/Ar mixed atmosphere at 450 °C for 3 h. The resulting samples with 1, 3, 10, and 20 wt % Ni loadings were labeled as Ni_1/CeO_2, Ni_3/CeO_2, Ni_{10}/CeO_2, and Ni_{20}/CeO_2, respectively.

Synthesis of Ni_{10}/CeO_2−A, Ni_{10}/CeO_2−B, and Ni_{10}/CeO_2−C Photocatalysts. The Ni_{10}/CeO_2−A, Ni_{10}/CeO_2−B, and Ni_{10}/CeO_2−C photocatalysts were synthesized using a protocol analogous to that of the Ni/CeO_2 photocatalysts, with the CeO_2 substrate replaced by CeO_2-Type A (CeO_2−A), CeO_2-Type B (CeO_2−B), and CeO_2−Commercial (CeO_2−C), respectively. The Ni loading was maintained at 10 wt % for all three samples.

Materials Characterization. X-ray photoelectron spectroscopy (XPS) was performed on the synthesized powders using a Thermo Scientific K-Alpha spectrometer to analyze surface binding energies. All peaks were energy-calibrated against the C 1s peak of adventitious carbon at 284.8 eV. Raman spectra were acquired with a Horiba Scientific LabRAM HR Evolution system equipped with a 532 nm argon-ion laser as the excitation source. Morphological details were observed by transmission electron microscopy (TEM) on a FEI Talos F200x, and high-angle annular dark-field (HAADF) imaging coupled with energy-dispersive X-ray spectroscopy (EDX) was conducted using the integrated Super-X detector. Aberration-corrected scanning transmission electron microscopy (STEM) was carried out on a JEM-ARM200F at 200 kV. X-ray diffraction (XRD) analysis was carried out on a Rigaku Ultima IV diffractometer with Cu Kα radiation. The Ni content in the reduced catalysts was quantified by inductively coupled plasma optical emission spectroscopy (ICP-OES) on a PE Avio 200 spectrometer. Optical properties were measured using a UV-3600i Plus ultraviolet−visible-near-infrared spectrophotometer. Electron paramagnetic resonance (EPR) spectroscopy was performed on a Bruker EMXplus to analyze oxygen vacancies. H_2-TPR, CO_2-TPD and CH_4-TPD experiments were conducted on a BelCat II analyzer. In situ DRIFTS during adsorption and reaction stages was monitored using a Bruker Tensor II spectrometer. Surface temperature under light irradiation was detected with a FILR infrared thermal imaging camera. Time-resolved photoluminescence (TRPL) decay curves were recorded on an FLS-1000 transient fluorescence spectrometer with a 350 nm excitation wavelength.

$$y = A + B_1\exp(-t/\tau_1) + B_2\exp(-t/\tau_2) \quad (1)$$

Photocatalytic Performance Evaluation. The reaction was conducted in a Perfect 6A circulation system (100 mL) and a custom U-shaped quartz reactor (45 mL). A 300 W xenon lamp (CEL-HXUV300-T3, Beijing China Education AuLight Technology Co., Ltd.) with a wavelength range of 200−2500 nm served as the light source, maintaining a constant light intensity of 1.5 W cm^{-2} (detected by CEL-NP2000-2A, Beijing China Education AuLight Technology Co., Ltd.). For each test, 20 mg of photocatalyst was placed in the U-shaped quartz reactor and evacuated to 10^{-2} Pa using a rotary pump for 1 h. Subsequently, the catalyst was in situ reduced under a 10% H_2/Ar atmosphere at 450 °C for 30 min, followed by immediate evacuation of the reactor for 5 min while hot to prevent gas adsorption. The reactor was then filled with a mixed reaction gas at 64 kPa (5% CO_2, 45% H_2 and 50% Ar), and the reaction was initiated under light irradiation for at least 4 h. Reaction products were analyzed by an online gas chromatograph (GC9720II, Fuli Instruments, China) using Ar (0.40 MPa, purity >99.999%) as the carrier gas. Quantitative analysis was performed with a flame ionization detector (FID) and a thermal conductivity detector (TCD). TON is defined as the ratio of the moles of CO_2 converted to CH_4 to the total moles of active metal sites in the reactor

$$\mathrm{TON} = \frac{n_{CH4}}{n_{metal}}$$

DFT Calculation. DFT calculations were performed using the projector augmented wave (PAW) method with the Vienna ab initio Simulation Package (VASP) simulation package. The interaction between the ionic cores and the valence electrons are described with the PAW method. The exchange and correlation interactions are described using the Perdew−Burke−Ernzerh of generalized gradient approximation (GGA). The cutoff energy is set to 400 eV for all calculations, and the convergence criterion of energy and force are 10^{-4} eV and 0.001 eV/Å, respectively. Besides, a 1 × 1 × 1 Gamma-centered *k*-point mesh is used for optimization of geometric structure and other calculations of the Ni/CeO_2(110) and Ni/CeO_2(111). To obtain the relaxed CeO_2 and Ni_{13} surface structures for constructing the Ni/CeO_2 interface, the unit cells were cleaved along the (110) and (110) planes of the CeO_2 bulk. We added a 15 Å vacuum layer along the *c*-axis, which is necessary to consider the influence of the periodic boundary conditions. Meanwhile, the Ni_{13} cluster was constructed and positioned on the CeO_2 (110) and (111) surfaces. Finally, the adsorption energies (E_{ads}) were calculated as $E_{ads} = E_{ad/sub} - E_{ad} - E_{sub}$, where $E_{ad/sub}$ is the total energies of the optimized adsorbate/substrate system, E_{ad} is the adsorbate in the gas phase, and E_{sub} is the clean substrate, respectively. The free energy (ΔG) for elemental reaction step were calculated as $\Delta G = \Delta E + \Delta E_{ZPE} - T\Delta S$, where ΔE is the difference between the total energy, ΔE_{ZPE} and ΔS are the differences in the zero-point energy and the change of entropy, T is the temperature (T = 298.15 K in this work), respectively.

ASSOCIATED CONTENT

Supporting Information

The Supporting Information is available free of charge at https://pubs.acs.org/doi/10.1021/acsnano.5c12967.

Includes XRD, TPR pro-files, EXAFS fitting curves, TEM and STEM images, XPS, EPR and Raman spectra, UV−visible absorption spectra, infrared thermo-grams, in situ DRIFTS spectra, TPD patterns, and computational models employed in DFT calculations (PDF)

AUTHOR INFORMATION

Corresponding Authors

Hui Song − *Advanced Catalytic Materials Research Center, School of Material Science and Engineering, Tianjin University, Tianjin 300072, P. R. China;* orcid.org/0000-0001-6424-7959; Email: hui.song@tju.edu.cn

https://doi.org/10.1021/acsnano.5c12967
ACS Nano 2025, 19, 38004−38015

Jinlu He − *College of Chemistry and Chemical Engineering, Inner Mongolia University, Hohhot 010021, P. R. China;* orcid.org/0000-0001-9772-8572; Email: hejinlu@imu.edu.cn

Hongwei Zhang − *Key Laboratory of Development and Application of Rural Renewable Energy, Biogas Institute of Ministry of Agriculture and Rural Affairs, Chengdu 610041, P. R. China;* orcid.org/0000-0002-6773-8769; Email: zhw9590@163.com

Authors

Xiaolei Guo − *College of Chemistry and Chemical Engineering, Inner Mongolia University, Hohhot 010021, P. R. China; Key Laboratory of Development and Application of Rural Renewable Energy, Biogas Institute of Ministry of Agriculture and Rural Affairs, Chengdu 610041, P. R. China*

Yuqi Wu − *College of Chemistry and Chemical Engineering, Inner Mongolia University, Hohhot 010021, P. R. China*

Yuhang Shao − *Key Laboratory of Development and Application of Rural Renewable Energy, Biogas Institute of Ministry of Agriculture and Rural Affairs, Chengdu 610041, P. R. China*

Shengrong Zhou − *Key Laboratory of Development and Application of Rural Renewable Energy, Biogas Institute of Ministry of Agriculture and Rural Affairs, Chengdu 610041, P. R. China*

Yasuo Izumi − *Department of Chemistry, Graduate School of Science, Chiba University, Inage-ku, Chiba 263-8522, Japan;* orcid.org/0000-0001-8366-1864

Liangwei Deng − *Key Laboratory of Development and Application of Rural Renewable Energy, Biogas Institute of Ministry of Agriculture and Rural Affairs, Chengdu 610041, P. R. China;* orcid.org/0000-0001-5288-9380

Wenguo Wang − *Key Laboratory of Development and Application of Rural Renewable Energy, Biogas Institute of Ministry of Agriculture and Rural Affairs, Chengdu 610041, P. R. China*

Complete contact information is available at: https://pubs.acs.org/10.1021/acsnano.5c12967

Author Contributions

⊥X.G. and Y.W. contributed equally. The manuscript was written through contributions of all authors. All authors have given approval to the final version of the manuscript.

Notes

The authors declare no competing financial interest.

ACKNOWLEDGMENTS

The authors are grateful for the financial support from National Natural Science Foundation of China (22209086, 22363007), Central Public-Interest Scientific Institution Basal Research Fund (1610012022006_03104), the Youth Innovation Program of Chinese Academy of Agricultural Sciences (Y2023QC33), The Agricultural Science and Technology Innovation Program (CAAS-ASTIP-ZDRW202510, CAAS-ASTIP-2021-BIOMA), China Agriculture Research System of MOF and MARA (CARS-35), Sichuan Science and Technology Program (2023YFH0056). The author gratefully acknowledges the members of Y.I.'s research group for their support in the synchrotron radiation XAFS measurements (2022G527).

REFERENCES

(1) Chen, Y.; Zhang, Y.; Fan, G.; Song, L.; Jia, G.; Huang, H.; Ouyang, S.; Ye, J.; Li, Z.; Zou, Z. Cooperative Catalysis Coupling Photo-/Photothermal Effect to Drive Sabatier Reaction with Unprecedented Conversion and Selectivity. *Joule* **2021**, *5*, 3235−3251.

(2) Zhang, Z.; Han, X.; Zhang, J.; Dong, Y.; Zhao, J.; Xu, Q.; Zhang, N. Revolutionizing Photothermal CO_2 Hydrogenation with Ceria-Based Catalysts. *Nano Res.* **2025**, *18*, 94906998.

(3) Yan, X.; Sun, W.; Fan, L.; Duchesne, P. N.; Wang, W.; Kübel, C.; Wang, D.; Kumar, S. G. H.; Li, Y. F.; Tavasoli, A.; Wood, T. E.; Hung, D. L. H.; Wan, L.; Wang, L.; Song, R.; Guo, J.; Gourevich, I.; Ali, F. M.; Lu, J.; Li, R.; Hatton, B. D.; Ozin, G. A. Nickel@Siloxene Catalytic Nanosheets for High-Performance CO_2 Methanation. *Nat. Commun.* **2019**, *10*, 2608.

(4) Jing, R.; Lu, X.; Wang, J.; Xiong, J.; Qiao, Y.; Zhang, R.; Yu, Z. CeO_2 -Based Frustrated Lewis Pairs via Defective Engineering: Formation Theory, Site Characterization, and Small Molecule Activation. *Small* **2024**, *20*, 2310926.

(5) Zhang, S.; Xia, Z.; Zou, Y.; Cao, F.; Liu, Y.; Ma, Y.; Qu, Y. Interfacial Frustrated Lewis Pairs of CeO_2 Activate CO_2 for Selective Tandem Transformation of Olefins and CO_2 into Cyclic Carbonates. *J. Am. Chem. Soc.* **2019**, *141*, 11353−11357.

(6) Li, W.; Gan, J.; Liu, Y.; Zou, Y.; Zhang, S.; Qu, Y. Platinum and Frustrated Lewis Pairs on Ceria as Dual-Active Sites for Efficient Reverse Water-Gas Shift Reaction at Low Temperatures. *Angew. Chem., Int. Ed.* **2023**, *62*, No. e202305661.

(7) Yu, J.; Qin, X.; Yang, Y.; Lv, M.; Yin, P.; Wang, L.; Ren, Z.; Song, B.; Li, Q.; Zheng, L.; Hong, S.; Xing, X.; Ma, D.; Wei, M.; Duan, X. Highly Stable Pt/CeO_2 Catalyst with Embedding Structure toward Water−Gas Shift Reaction. *J. Am. Chem. Soc.* **2024**, *146*, 1071−1080.

(8) Leybo, D.; Etim, U. J.; Monai, M.; Bare, S. R.; Zhong, Z.; Vogt, C. Metal−Support Interactions in Metal Oxide-Supported Atomic, Cluster, and Nanoparticle Catalysis. *Chem. Soc. Rev.* **2024**, *53*, 10450−10490.

(9) Wang, T.; Hu, J.; Ouyang, R.; Wang, Y.; Huang, Y.; Hu, S.; Li, W.-X. Nature of Metal-Support Interaction for Metal Catalysts on Oxide Supports. *Science* **2024**, *386*, 915−920.

(10) Jiang, M.; Chen, X.; Wang, L.; Liang, J.; Wei, X.; Nong, W. Anchoring Single Ni Atoms on CeO_2 Nanospheres as an Efficient Catalyst for the Hydrogenolysis of Lignin to Aromatic Monomers. *Fuel* **2022**, *324*, 124499.

(11) Xia, H.; Dang, C.; Zhou, D.; Cai, W. Lamellar Cross-Linking Ni/CeO_2 as an Efficient and Durable Catalyst for Dry Reforming of Methane. *Chem. Eng. J.* **2024**, *489*, 151365.

(12) Muravev, V.; Parastaev, A.; Van Den Bosch, Y.; Ligt, B.; Claes, N.; Bals, S.; Kosinov, N.; Hensen, E. J. M. Size of Cerium Dioxide Support Nanocrystals Dictates Reactivity of Highly Dispersed Palladium Catalysts. *Science* **2023**, *380*, 1174−1179.

(13) Xie, Y.; Chen, J.; Wu, X.; Wen, J.; Zhao, R.; Li, Z.; Tian, G.; Zhang, Q.; Ning, P.; Hao, J. Frustrated Lewis Pairs Boosting Low-Temperature CO_2 Methanation Performance over Ni/CeO_2 Nanocatalysts. *ACS Catal.* **2022**, *12*, 10587−10602.

(14) Raziq, F.; Feng, C.; Hu, M.; Zuo, S.; Rahman, M. Z.; Yan, Y.; Li, Q.-H.; Gascon, J.; Zhang, H. Isolated Ni Atoms Enable Near-Unity CH_4 Selectivity for Photothermal CO_2 Hydrogenation. *J. Am. Chem. Soc.* **2024**, *146* (30), 21008−21016.

(15) Li, Q.; Wang, C.; Wang, H.; Chen, J.; Chen, J.; Jia, H. Disclosing Support-Size-Dependent Effect on Ambient Light-Driven Photothermal CO_2 Hydrogenation over Nickel/Titanium Dioxide. *Angew. Chem., Int. Ed.* **2024**, *63*, No. e202318166.

(16) Rao, Z.; Wang, K.; Cao, Y.; Feng, Y.; Huang, Z.; Chen, Y.; Wei, S.; Liu, L.; Gong, Z.; Cui, Y.; Li, L.; Tu, X.; Ma, D.; Zhou, Y. Light-Reinforced Key Intermediate for Anticoking To Boost Highly Durable Methane Dry Reforming over Single Atom Ni Active Sites on CeO_2. *J. Am. Chem. Soc.* **2023**, *145*, 24625−24635.

(17) Zheng, H.; Liao, W.; Ding, J.; Xu, F.; Jia, A.; Huang, W.; Zhang, Z. Unveiling the Key Factors in Determining the Activity and

Selectivity of CO_2 Hydrogenation over Ni/CeO_2 Catalysts. *ACS Catal.* **2022**, *12*, 15451−15462.
(18) Zhang, K.; Meng, Q.; Wu, H.; Yan, J.; Mei, X.; An, P.; Zheng, L.; Zhang, J.; He, M.; Han, B. Selective Hydrodeoxygenation of Aromatics to Cyclohexanols over Ru Single Atoms Supported on CeO_2. *J. Am. Chem. Soc.* **2022**, *144*, 20834−20846.
(19) Mi, R.; Li, D.; Hu, Z.; Yang, R. T. Morphology Effects of CeO_2 Nanomaterials on the Catalytic Combustion of Toluene: A Combined Kinetics and Diffuse Reflectance Infrared Fourier Transform Spectroscopy Study. *ACS Catal.* **2021**, *11*, 7876−7889.
(20) Shirayama, K.; Jin, X.; Nozaki, K. Selective Hydrogenation of Aldehydes under Syngas Using CeO_2-Supported Au Nanoparticle Catalyst. *J. Am. Chem. Soc.* **2024**, *146*, 14086−14094.
(21) Yang, Z.; Huang, T.; Li, M.; Wang, X.; Zhou, X.; Yang, S.; Gao, Q.; Cai, X.; Liu, Y.; Fang, Y.; Wang, Y.; Zhang, S.; Zhang, S. Unveiling the Synergistic Role of Frustrated Lewis Pairs in Carbon-Encapsulated Ni/NiO_x Photothermal Cocatalyst for Enhanced Photocatalytic Hydrogen Production. *Adv. Mater.* **2024**, *36*, 2313513.
(22) Wang, H.; Li, Q.; Chen, J.; Chen, J.; Jia, H. Efficient Solar-Driven CO_2 Methanation and Hydrogen Storage Over Nickel Catalyst Derived from Metal−Organic Frameworks with Rich Oxygen Vacancies. *Adv. Sci.* **2023**, *10*, 2304406.
(23) Liu, P.; Zheng, C.; Liu, W.; Wu, X.; Liu, S. Oxidative Redispersion-Derived Single-Site Ru/CeO_2 Catalysts with Mobile Ru Complexes Trapped by Surface Hydroxyls Instead of Oxygen Vacancies. *ACS Catal.* **2024**, *14*, 6028−6044.
(24) Wang, Z.; Zhu, J.; Zu, X.; Wu, Y.; Shang, S.; Ling, P.; Qiao, P.; Liu, C.; Hu, J.; Pan, Y.; Zhu, J.; Sun, Y.; Xie, Y. Selective CO_2 Photoreduction to CH_4 via $Pd^{\delta+}$-Assisted Hydrodeoxygenation over CeO_2 Nanosheets. *Angew. Chem., Int. Ed.* **2022**, *61*, No. e202203249.
(25) Wang, Y.; Cai, J.; Wu, M.; Chen, J.; Zhao, W.; Tian, Y.; Ding, T.; Zhang, J.; Jiang, Z.; Li, X. Rational Construction of Oxygen Vacancies onto Tungsten Trioxide to Improve Visible Light Photocatalytic Water Oxidation Reaction. *Appl. Catal., B* **2018**, *239*, 398−407.
(26) Zhang, Y.-P.; Han, W.; Yang, Y.; Zhang, H.-Y.; Wang, Y.; Wang, L.; Sun, X.-J.; Zhang, F.-M. S-Scheme Heterojunction of Black TiO_2 and Covalent-Organic Framework for Enhanced Photocatalytic Hydrogen Evolution. *Chem. Eng. J.* **2022**, *446*, 137213.
(27) Qi, Y.; Jiang, J.; Liang, X.; Ouyang, S.; Mi, W.; Ning, S.; Zhao, L.; Ye, J. Fabrication of Black In_2O_3 with Dense Oxygen Vacancy through Dual Functional Carbon Doping for Enhancing Photothermal CO_2 Hydrogenation. *Adv. Funct. Mater.* **2021**, *31*, 2100908.
(28) Guo, C.; Tang, Y.; Yang, Z.; Zhao, T.; Liu, J.; Zhao, Y.; Wang, F. Reinforcing the Efficiency of Photothermal Catalytic CO_2 Methanation through Integration of Ru Nanoparticles with Photothermal $MnCo_2O_4$ Nanosheets. *ACS Nano* **2023**, *17*, 23761−23771.
(29) Xiong, Y.; Liu, X.; Hu, Y.; Gu, D.; Jiang, M.; Tie, Z.; Jin, Z. $Ag_{24}Au$ Cluster Decorated Mesoporous Co_3O_4 for Highly Selective and Efficient Photothermal CO_2 Hydrogenation. *Nano Res.* **2022**, *15*, 4965−4972.
(30) Köck, E.-M.; Kogler, M.; Bielz, T.; Klötzer, B.; Penner, S. In Situ FT-IR Spectroscopic Study of CO_2 and CO Adsorption on Y_2O_3, ZrO_2, and Yttria-Stabilized ZrO_2. *J. Phys. Chem. C* **2013**, *117*, 17666−17673.
(31) Li, T.; Zhang, Z.-Y.; Luo, D.-C.; Xu, B.-Y.; Zhang, R.-J.; Yao, J.-L.; Li, D.; Xie, T. Highly Efficient Photo-Thermal Synergistic Catalysis of CO_2 Methanation over La1−xCexNiO3 Perovskite-Catalyst. *Nano Res.* **2024**, *17*, 7945−7956.
(32) Li, Y.; Liu, Z.; Rao, Z.; Yu, F.; Bao, W.; Tang, Y.; Zhao, H.; Zhang, J.; Wang, Z.; Li, J.; Huang, Z.; Zhou, Y.; Li, Y.; Dai, B. Experimental and Theoretical Insights into an Enhanced CO2Methanation Mechanism over a Ru-Based Catalyst. *Appl. Catal., B* **2022**, *319*, 121903.
(33) Zhang, H.; Itoi, T.; Konishi, T.; Izumi, Y. Efficient and Selective Interplay Revealed: CO_2 Reduction to CO over ZrO_2 by Light with Further Reduction to Methane over Ni^0 by Heat Converted from Light. *Angew. Chem., Int. Ed.* **2021**, *60*, 9045−9054.
(34) Ye, R.; Ma, L.; Hong, X.; Reina, T. R.; Luo, W.; Kang, L.; Feng, G.; Zhang, R.; Fan, M.; Zhang, R.; Liu, J. Boosting Low-Temperature CO_2 Hydrogenation over Ni-based Catalysts by Tuning Strong Metal-Support Interactions. *Angew. Chem., Int. Ed.* **2024**, *63*, No. e202317669.
(35) Qin, X.; Xu, M.; Guan, J.; Feng, L.; Xu, Y.; Zheng, L.; Wang, M.; Zhao, J.-W.; Chen, J.-L.; Zhang, J.; Xie, J.; Yu, Z.; Zhang, R.; Li, X.; Liu, X.; Liu, J.-X.; Zheng, J.; Ma, D. Direct Conversion of CO and H_2O to Hydrocarbons at Atmospheric Pressure Using a TiO_{2-x}/Ni Photothermal Catalyst. *Nat. Energy* **2024**, *9*, 154−162.
(36) Li, M.; He, C.; Yang, X.; Liu, Z.; Li, J.; Wang, L.; Wu, S.; Zhang, J. Optimizing Water Dissociation Dehydrogenation Process via Sn Single Atom Incorporation for Boosting Photocatalytic CO_2 Methanation. *Chem Catal.* **2023**, *3*, 100737.
(37) Wang, C.; Lu, Y.; Zhang, Y.; Fu, H.; Sun, S.; Li, F.; Duan, Z.; Liu, Z.; Wu, C.; Wang, Y.; Sun, H.; Yan, Z. Ru-Based Catalysts for Efficient CO2Methanation: Synergistic Catalysis between Oxygen Vacancies and Basic Sites. *Nano Res.* **2023**, *16*, 12153−12164.
(38) Zhang, M.; Mao, Y.; Bao, X.; Wang, P.; Liu, Y.; Zheng, Z.; Cheng, H.; Dai, Y.; Wang, Z.; Huang, B. Promoting Photocatalytic CO_2 Methanation by the Construction of Cooperative Copper Dual-Active Sites. *ACS Catal.* **2024**, *14*, 5275−5285.

https://doi.org/10.1021/acsnano.5c12967
ACS Nano 2025, 19, 38004−38015